**Effects of Temperature and Humidification Levels on the Performance of a Proton Exchange Membrane Fuel Cell**

M-S Chiang and H-S Chu

The online version of this article can be found at:

http://pia.sagepub.com/content/220/5/435

Published by:

$SAGE

http://www.sagepublications.com

On behalf of:

Institution of Mechanical Engineers

Institution of Mechanical Engineers

**Additional services and information for _Proceedings of the Institution of Mechanical Engineers, Part A: Journal of Power and Energy_ can be found at:**

**Email Alerts:** http://pia.sagepub.com/cgi/alerts

**Subscriptions:** http://pia.sagepub.com/subscriptions

**Reprints:** http://www.sagepub.com/journalsReprints.nav

**Permissions:** http://www.sagepub.com/journalsPermissions.nav

**Citations:** http://pia.sagepub.com/content/220/5/435.refs.html

>> Version of Record - Aug 1, 2006

What is This?

# Effects of temperature and humidification levels on the performance of a proton exchange membrane fuel cell

**M-S Chiang**[1,2*] and **H-S Chu**[1]

[1]Department of Mechanical Engineering, National Chiao Tung University, Hsinchu, Taiwan, Republic of China
[2]Department of Mechanical Engineering, Nan Kai Institute of Technology, Nantou, Taiwan, Republic of China

**Abstract:** Numerical investigation of a proton exchange membrane fuel cell performance subjected to various humidification and thermal conditions is the focus of this study. Governing equations describing species, mass, momentum, and enthalpy conservation are employed and solved by a computational fluid dynamic algorithm to obtain domain's physical properties and cell performance. The model accounts for electrochemical kinetic as well as two-phase flow with phase change and water transport. Numerical prediction results use polarization curves and contour plots to illustrate the effects of various humidification schemes and temperature gradient scenarios. Findings show that humidification-level perturbation on the anode or cathode side creates different effects. Mechanisms influencing performance-variation tendencies are interpreted. In addition modelling results with existing temperature gradient exhibit different trends on the overpotentials depending on the slope and magnitude. At higher cathode temperature, it is shown that polarization curves are dominated by reaction kinetics and membrane water content at medium and high reaction rates, respectively.

**Keywords:** proton exchange membrane fuel cell, water and thermal management, humidification level, temperature gradient

## 1 INTRODUCTION

Fuel cell systems convert fuel chemical energy directly into electrical energy. When a traditional thermal engine combustion process is replaced by an electrochemical reaction, it has advantages of quietness, high efficiency, low emission, and simplicity. Given these characteristics, the fuel cell is a revolutionary 21st century power conversion device with applications to vehicles, electronic equipments, and other stationary power generation systems. The proton exchange membrane fuel cell (PEMFC), using solid polymers as working ions' passages, has recently received much attention and intensive study as a promising candidate of these applications [1].

During the fuel cell power conversion process, chemical energy stored in the bounded atom electronic orbits is liberated and converged into electrical energy through electrocatalytic activity of catalysts in the electrodes. Catalysts macroscopically liberate electrons of hydrogen molecules which are converted into protons simultaneously at the anode. These two charged species are transported through individual gateways by electric field functions and other mechanisms. The electrons move along the external circuit and release electrical energy through potential drop on the loading. Proton transport is driven by a set of more complicated factors. The proton exchange membrane (PEM) must be hydrated for ion movement facilitation. It uses polytetrafluoroethylene as the structure backbone and sulphonic acid side chains for the ion conduction purpose. Although proton movement in the membrane is not well understood, suitable membrane water content is beneficial [2]. Additionally, with polar molecular property, water is carried by protons and moved from the anode to the cathode during cell operation. Concentration and pressure gradients through the membrane also have a degree of influence on water transport.

---

*Corresponding author: Department of Mechanical Engineering, National Chiao Tung University, Room 342, Engineering Building No. 5, 1001 Ta Hsuch Road, Hsinchu, Taiwan 300, Republic of China. email: sam@nkc.edu.tw*

Water is produced in the cathode catalyst layer (CL) because of cell reaction and, with the aforementioned effects, may lead to a flooding problem and dramatically reduce cell performance at high current density. Several works performed on this issue propose a better understanding and fulfilling of fuel cell system water management [3–6]. The temperature factor is inevitable in water management investigation because water phase change closely relates to corresponding saturation pressure and relative humidity. The energy fraction released by heat during cell operation is as high as 50 per cent of the total energy used at high current densities, such that there is an equal amount of thermal energy produced accompanying the power generated. The extra high temperature might lead to membrane dehydration and poor ion transport without imposing special effort. On the contrary, when the electrode temperature is high, vapour saturation pressure is elevated with reduced relative humidity, preventing water formation and a further flooding problem.

Transport and energy conversion processes in the PEMFC involve multi-phase, multi-component flow and heat and mass transfer in porous media with electrochemical reactions. Reactants are delivered and distributed evenly by grooved flow channels on bipolar plates (BPs). Despite the simple geometry of flow channels, the actual flow field is intrinsically three-dimensional that contains longitudinal, transverse, and through plane directions. The cathode CL serves as oxygen sink and water source. The most challenging aspect of modelling the fuel cell transport phenomena is that these processes are coupled with complex electrochemical reactions.

Bernardi and [7], Bernardi and Verbrugge [8, 9], Springer et al. [10] pioneered the study of PEMFC modelling, which utilized the lump approach and the conservation theory to develop unidirectional models through electrodes and membrane assuming isothermal condition. The Bernardi model [7] suggested reactant gas humidification tuning to accommodate changing cell demands for water. Springer et al. [10] utilized their model to study the water transport coefficient and cell performance for different anode humidifier temperatures. Fuller and Neuman [11] considered a two-dimensional membrane–electrode assembly and examined the water thermal management in PEMFC. Membrane water concentration and gas channel temperature were calculated for different heat transfer coefficients. Findings showed that a lower heat transfer coefficient is responsible for membrane dehydration and substantial cell performance decrease. Yi and Nguyen [12] developed an along-the-channel, two-dimensional model including various thermal management schemes. Their model results showed that

the heat exchanger design with counter flow is more effective than coflow and constant bulk temperature schemes. Besides these works, the model of Rowe and Li [13] included variable membrane hydration and water phase change in the electrodes. Baschuk and Li [14] investigated variable degree effect of water flooding in the CL layer and/or cathode electrode backing region on cell performance. Simpalee and Dutta [15] formulated a comprehensive three-dimensional model to predict temperature distribution inside a straight channel PEMFC and presented a group of source terms facilitating commercial software application. Djilali and Lu [16] analysed transport phenomena in a PEMFC assessing non-isothermal and non-isobaric effects. Furthermore, numerical results of Ju et al. [17] with a single-phase and non-isothermal model revealed that temperature rise within the cell could be as high as 13.75 K at medium reaction rate under certain conditions.

It is clear from the above literature reviews that water and thermal management plays an essential role on the PEMFC performance. However, no studies have ever investigated the gradient influences of cell temperature and humidification level arising from transient cold start or inadequate cooling conditions. The purpose of this study is to present a systematic investigation of these two factor impacts on PEMFC polarization characteristics. Relationships between temperature and electrochemical kinetics, as well as membrane conductivity, are modelled using empirical formulas. Local temperature and relative humidity factors on water phase change and transport are harnessed in the modelling to evaluate their influences on cell outputs.

## 2  MATHEMATICAL FORMULATIONS

Various transport phenomena such as mass, momentum, and energy, as well as electrochemical reactions and phase change are coupled during the PEMFC power generation. Governing equations concerning these problems are introduced in the following. Figure 1 shows the physical and computational domain considered in this study consisting of BPs, gas diffusion layers (GDLs), CLs, and the PEM. Species contained in the anode region are hydrogen and water, whereas oxygen, nitrogen, and water are those in the cathode region.

The following assumptions are made for this study.

1. The calculated mixture compressibility factor is close to unity. Ideal gas behaviour is assumed for anode and cathode gas mixtures.
2. Owing to low reactant velocity, the Reynolds number is usually below 100 and the laminar
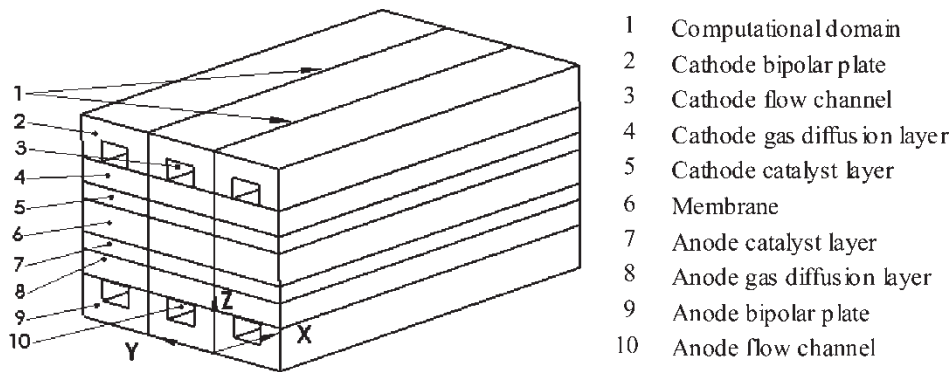
Fig. 1 Physical and computational domain considered in this study

| 1 | Computational domain |
| 2 | Cathode bipolar plate |
| 3 | Cathode flow channel |
| 4 | Cathode gas diffusion layer |
| 5 | Cathode catalyst layer |
| 6 | Membrane |
| 7 | Anode catalyst layer |
| 8 | Anode gas diffusion layer |
| 9 | Anode bipolar plate |
| 10 | Anode flow channel |

flow assumption is made for the fluid in the domain.

3. Transport properties in the porous media are isotropic and phase compositions in mixture are smoothly varying.

4. The electric potentials on top and bottom of the cell are constant.

5. The pressure diffusion, thermal diffusion, and Knudsen effect are not considered in species mass transport.

6. Working fluid and the porous media solid phase are in local thermal equilibrium.

7. There is no charge accumulation in the electrodes and the electroneutrality assumption is made in the domain.

## 2.1 Mass conservation of species and bulk mixture

The mass fraction of individual species in the domain can be described as

$$\nabla \cdot (\varepsilon \rho w_\alpha \boldsymbol{U} \lambda_g) = \nabla \cdot \left( \rho \sum_{\beta=1}^{n-1} \boldsymbol{D}_{\alpha\beta} \nabla w_\beta \right) + S_{s,\alpha} \qquad (1)$$

where $\alpha$ and $\beta$ denote the individual species that represent oxygen, hydrogen, nitrogen, and water, $\varepsilon$ is the effective porosity corrected by the saturation level, $\rho$ the bulk density of the mixture, and $w_\alpha$ the mass fraction of species $\alpha$. The equation source term connects the mass transport and electrochemical reaction in CLs. The consumption or creation of each species depends on the local volume-based current density divided by the Faraday constant and electron numbers transferred. Note that the gas phase relative mobility $\lambda_g$ is employed in the convection term of equation (1) to consider the two-phase flow phenomenon.

The multi-component diffusion coefficient $\boldsymbol{D}_{\alpha\beta}$ is a function of species concentration and binary diffusion coefficient, the latter can be written as [18, 19]

$$D_{\gamma\delta} = \frac{0.0018583\big[T^{3/2}(1/M_\gamma + 1/M_\delta)^{1/2}\big]}{P\psi_{\gamma\delta}\Omega_{\gamma\delta}} \varepsilon^\delta \qquad (2)$$

where $T$ is the temperature in kelvin, $P$ the pressure in atm, and $M_\gamma$ the molecular weight of species $\gamma$. The parameters in the denominator $\psi_{\gamma\delta}$ and $\Omega_{\gamma\delta}$ are the collision diameter and the collision integral between species $\gamma$ and $\delta$.

The densities of species and bulk fluid have the relation

$$\rho = \sum_{\alpha=1}^{n} \rho_\alpha (1 - s) + \rho_l s \qquad (3)$$

where $s$ is the saturation level of the liquid phase and the following continuity equation describes the mass conservation of mixture

$$\nabla \cdot (\varepsilon \rho \boldsymbol{U}) = 0 \qquad (4)$$

## 2.2 Momentum equation

The general form of Navier–Stokes equation is employed with source terms to account for drag forces arising in the porous region. The equation is given as

$$\nabla \cdot (\rho \varepsilon \boldsymbol{U}\boldsymbol{U}) = -\varepsilon \nabla P + \nabla \cdot (\varepsilon \mu^{\text{eff}} \nabla \cdot \boldsymbol{U}) + S_{\text{m}} \qquad (5)$$

where $\mu^{\text{eff}}$ is the effective viscosity of reaction mixtures in anode and cathode and $S_{\text{m}}$ represents the Darcy and Forchheimer terms that describe the momentum dissipation in the porous media. Their expressions are

$$\mu^{\text{eff}} = \frac{\rho_l s + \rho_g (1 - s)}{(k_{\text{rl}}/\nu_l) + (k_{\text{rg}}/\nu_g)} \qquad (6)$$

$$S_{\text{m}} = -\frac{\varepsilon^2 \boldsymbol{U}}{\sqrt{K}} \left( \frac{\mu^{\text{eff}}}{\sqrt{K}} + \varepsilon C_F \rho |\boldsymbol{U}| \right) \qquad (7)$$

where $K$ is the permeability and $C_F$ is the form drag constant. Equation (5) is restored to the original Navier–Stokes Equation by setting porosity $\varepsilon$ equal to unity and $K$ approach infinity in flow channel regions. At the other place, the convection term and diffusion term drop out because the permeability in the denominator is extremely small. Employing a unified formulation in different transport property regions is advantageous, as there is no need of dealing with the interface condition of physical property continuity used in early works [17, 20].

## 2.3 Energy equation

Energy equation is important in this study, as it describes the thermal energy conservation in the domain and the temperature field can be extracted from it. Except for inlet and outlet boundaries, enthalpy generation is considered from three sources: joule heating due to current transport in the medium, electrochemical reaction irreversibility due to overpotential at electrodes, and latent heat of water due to phase change. Many physical properties are closely related to temperature in the cell domain. First, mixture velocities at channel inlet ports for a fixed reactant stoichiometry and a given cell geometry are primarily decided by their thermodynamic states and subsequently dictated by mixture temperatures. Secondly, electrochemical reaction kinetics in the CL and membrane conductivity are also influenced by local temperatures. Thirdly, the temperature field is also responsible for water formation or evaporation. Consequently, it has certain effects on reactant concentration and membrane water content. The generalized steady-state energy equation can be expressed as

$$\nabla \cdot (\varepsilon \rho h U) = \nabla \cdot \left( \kappa^{\text{eff}} \nabla T + \sum_{\alpha=1}^{n} \sum_{\beta=1}^{n-1} \rho D_{\alpha\beta} \nabla w_{\beta} h_{\alpha} \right) + \varepsilon \tau \colon \nabla U - S_j \eta + \frac{|i \cdot i|}{\sigma} + S_h \quad (8)$$

where the first two terms on the right-hand side represent the conduction energy and reactant enthalpy flux and the third term is the irreversible viscous dissipation. The fourth and the fifth terms describe the electrical-related thermal effects, where $S_j$ is the volumetric current density in the CL that can be expressed by the Bulter–Volmer equation shown in section 2.5. The last term results from the consideration of phase change when water evaporation or condensation occurs in the cell domain and is presented in the next section following the phase change formulation.

## 2.4 Formation and transport of water

Water vapour partial pressure varies from channel inlet to outlet, as cell reactions alter its concentration. Water forms as a result, when local relative humidity is greater than 1. On the contrary, the water evaporation process activates as soon as relative humidity is less than 1 and water exists. The generalized Richards equation developed by Wang and Cheng [21] is employed to mimic water transport in the cell domain. This equation essentially originates from water mass conservation in a control volume. It can be given as

$$\nabla \cdot (\varepsilon \rho U \lambda_l) + \nabla \cdot N_l \\ = \nabla \cdot \left( \varepsilon \rho_l D^c \nabla s - \frac{\lambda_l \lambda_g K (\rho_l - \rho_g) g}{\nu} \right) + S_l \quad (9)$$

In equation (a), the electro-osmotic drag effect is included using a divergent expression of water mass flux with a drag coefficient of 2.5 s [22]. The diffusion coefficient of water $D^c$ is subjected to capillary pressure and, in turn, controlled by surface tension and water saturation level [23]

$$D^c = -\frac{s^3 K (1 - \lambda_l)(dP^c/ds)}{\mu_l} \quad (10)$$

$$P^c = \varsigma \cos \theta^c \left( \frac{\varepsilon}{K} \right)^{1/2} [1.417(1-s) \\ - 2.12(1-s)^2 + 1.262(1-s)^3] \quad (11)$$

where $\lambda_l$ is the liquid phase mobility given by relative permeability and kinetic viscosity

$$\lambda_l = \frac{k_{rl}/\nu_l}{k_{rl}/\nu_l + k_{rg}/\nu_g} \quad (12)$$

Water condensation or evaporation is considered by introducing the source term $S_l$ in equation (9) as [24]

$$S_l = \begin{cases} M_l r_{con} \frac{\varepsilon x_w}{RT}(x_w P - P_{sat}), & \text{if} \quad x_w P > P_{sat} \\ r_{eva} \varepsilon s \rho_l (x_w P - P_{sat}), & \text{if} \quad x_w P < P_{sat} \end{cases} \quad (13)$$

where $r_{con}$ and $r_{eva}$ represent phase change rate constants. Owing to this process, the source term $S_h$ in equation (8) can be obtained by multiplying $S_l$ with water latent heat.

## 2.5 Cell potential and electrochemical reaction

When current is drawn from the cell, two charged species move along individual paths by the potential gradient effect. Conducting materials for electrons are the solid phases (carbon cloth or paper, carbon support, and catalyst particle) in CLs, GDLs, and

Proc. IMechE Vol. 220 Part A: J. Power and Energy

JPE180 © IMechE 2006

BPs (flow field plate). Proton transport media are the ionomer phases in membrane and CLs. Potential fields in these two media can be described as

$$\nabla \cdot (\sigma_{sol} \nabla \phi_{sol}) = S_j \tag{14}$$

$$\nabla \cdot (\sigma_{mem} \nabla \phi_{mem}) = -S_j \tag{15}$$

where $\sigma_{sol}$ and $\sigma_{mem}$ are the electrical conductivities of these two transport media and $\phi_{sol}$ and $\phi_{mem}$ are the aforementioned potential fields. The term $S_j$ represents the source or sink of the two currents. In the anode CL, they are created, and in the CL, they are consumed. The membrane conductivity $\sigma_{mem}$ is a vital property that exerts great influence on the cell performance. The model of Springer *et al.* [10] is used in this study

$$\sigma_{mem} = (0.005139\gamma - 0.00326)$$
$$\times \left\{ \exp\left[ 1268\left( \frac{1}{303} - \frac{1}{T} \right) \right] \right\} \tag{16}$$

where $\gamma$ is the membrane water content defined as the number of water molecules per sulphonic acid group and $T$ is the temperature.

The CL overpotential is the electrochemical reaction driving force, which is the difference between $\phi_{sol}$ and $\phi_{mem}$. The volumetric-based transfer current density considering electrode structure, reactant concentration, temperature, and overpotential is given by the Bulter–Volmer equation. It represents the heterogeneous catalyst reaction rate among reactants and solid platinum particles in an electrode. At open circuit voltage, anodic and cathodic currents occurred simultaneously. However, the overpotential biases the net current towards a favourite direction. Consequently, an oxygen reduction reaction in cathode or a hydrogen oxidation reaction in anode is activated. The equation is written as

$$S_{j,k} = A_v i_{ref,k} \left( \frac{c_\alpha}{c_{\alpha,ref}} \right)^{\varphi_\alpha}$$
$$\times \left[ \exp\left( \frac{\beta_{k,a} F \eta_k}{RT} \right) - \exp\left( \frac{-\beta_{k,c} F \eta_k}{RT} \right) \right] \tag{17}$$

where $A_v$ is the effective catalyst surface area per unit volume of CL, $i_{ref,k}$ the reference exchange current density, $c_\alpha$ the molar concentration of species $\alpha$, and $\beta_{k,a}$ and $\beta_{k,c}$ are the anodic and cathodic transfer coefficients at anode and cathode, respectively. Note that the CL contains nanoscale platinum particles distributed on carbon supports; its effective surface area is several orders of magnitude greater than the geometric area. The following expression provides the relation among $A_v$ and parameters

describing CL structure such as catalyst surface area per unit mass, catalyst loading, and layer thickness

$$A_v = \frac{A_{mas} m_{plt}}{H_{cat}} \tag{18}$$

The experimental results from Parthasarathy *et al.* [25] provide the relation between the cathode reference exchange current density and temperature

$$i_{ref,o2} = 10^4 \exp\left( 3.507 - \frac{4001}{T} \right) \tag{19}$$

### 2.6  Boundary condition

As this study investigates temperature gradient and humidification level impacts on cell performance, specific wall temperatures are prescribed at the top and bottom of the computational domain. Thus, the uneven temperature scenario during system start up, as well as in a cell stack unit, could be simulated. At the channel outlet port, a fixed back pressure is prescribed. The reactant temperature at channel inlet is made equal to the humidification level, and the mixture species concentration can readily be calculated from Dalton's law. With these data, anode or cathode mixture inlet velocity is decided by the following relation

$$v_k = \frac{\xi I W_{cel} L_{cha} R T_{k,in}}{q F W_{cha} H_{cha} (1 - P_{sat,w,k}/P_k) x_{\alpha,in} P_k} \tag{20}$$

where the subscript $\alpha$ refers to hydrogen at anode and oxygen at cathode, respectively; and $q$ equals 2 in anode flow and 4 in cathode flow.

Neumann boundary conditions are used on the symmetry walls and CL interfaces in contact with membrane and GDLs to ascertain thermal energy and electrical current flux impermeability. Fixed value of total cell overpotential is specified on the cathode outer boundary. This value includes ohmic overpotentials in electrodes and membrane, as well as activation overpotentials in CLs. With this method, membrane and solid-phase potential fields are obtained, and local current densities can be calculated from the ohmic law. Consequently, cell potential is obtained by subtracting total cell overpotential from open circuit voltage

$$\phi_{cel} = \phi_{oc} - \eta_{tot} \tag{21}$$

$$\phi_{oc} = 0.2329 + 0.0025 T_{cel} \tag{22}$$

The feature of such voltage-to-current algorithm is that it can be used to resolve CL local activation

overpotential [26], needed in the calculation of the Bulter–Volmer equation.

## 2.7 Numerical procedure

The governing equations were converted to the conservative convection–diffusion form and solved by the computational fluid dynamic algorithm with control volume approach [27–29], in which a staggered grid system was used for the velocity field. Momentum equations were solved first, and then the pressure and velocity fields were corrected to satisfy the continuity equation. Following the velocity vector, temperature field, species concentrations, potential fields, and saturation level were solved. Throughout the calculation procedure, proper under-relaxation factors were employed for numerical stability consideration. Main parameters and dimensions employed in this study are shown in Tables 1 and 2. The calculation process was iterated until the relative residual of each variable became smaller than $1 \times 10^{-4}$. Various grid systems with total cell numbers of 23 010, 53 600, 76 380, and 100 320 were constructed to evaluate the cell number dependence on output current density. The calculated data indicated that a cell number of 53 600 gave a satisfactory result, and the computational time was largely reduced when compared with the other two higher cell number systems. Simulations were performed on a personal computer with a Pentium IV 2.4 GHz CPU. It generally required $\sim$48 h to accomplish a typical polarization curve with 13 data points.

Model validation certification was conducted by comparing results with Wang et al.'s report [30], using their model dimensions and operating conditions as shown in Fig. 2. It discloses a satisfactory agreement between experimental and current modelling results at different operating temperatures.

**Table 1** Model dimensions and operating conditions of this study

| Parameters and properties | Value | Units |
|---|---|---|
| Domain length | $5.0 \times 10^{-2}$ | m |
| Domain width | $1.6 \times 10^{-3}$ | m |
| Gas channel width | $8.0 \times 10^{-4}$ | m |
| Domain height | $4.303 \times 10^{-3}$ | m |
| Gas channel height | $8.0 \times 10^{-4}$ | m |
| Diffusion layer thickness | $2.54 \times 10^{-4}$ | m |
| Catalyst layer thickness | $1.0 \times 10^{-6}$ | m |
| Membrane thickness | $1.75 \times 10^{-4}$ | m |
| Molar ratio of cathode side dry air ($N_2/O_2$) | 79/21 | |
| Anode $H_2$ stoichiometry | 3 | |
| Cathode $O_2$ stoichiometry | 3 | |
| Anode pressure | 2 | atm |
| Cathode pressure | 2 | atm |

**Table 2** Main physical parameters and properties utilized in this study

| Parameters and properties | Value | Units |
|---|---|---|
| Porosity of the diffusion and catalyst layer | 0.4 | |
| Porosity of the membrane | 0.28 | |
| Permeability of the diffusion and catalyst layer | $2.3 \times 10^{-11}$ | $m^2$ |
| Permeability of the membrane | $1.0 \times 10^{-18}$ | $m^2$ |
| Tortuosity of the diffusion and catalyst layer | 1.5 | |
| Tortuosity of the membrane | 3 | |
| Molar ratio of cathode side dry air ($N_2/O_2$) | 79/21 | |
| Collision diameter between $H_2$ and $H_2O$ | 2.734 | Å |
| Collision diameter between $O_2$ and $H_2O$ | 3.054 | Å |
| Collision diameter between $O_2$ and $N_2$ | 3.633 | Å |
| Collision diameter between $N_2$ and $H_2O$ | 3.220 | Å |
| Surface tension of water | 0.06253 | N/m |
| Contact angle | 0 | ° |
| Condensation rate constant | 100 | $s^{-1}$ |
| Evaporation rate constant | 100 | 1/atm s |
| Concentration dependence of $H_2$ | 0.5 | |
| Concentration dependence of $O_2$ | 1 | |
| Transfer coefficient at anode | 0.5 | |
| Transfer coefficient at cathode | 1.5 | |
| Electrical conductivity of electrode | 114 | $1/\Omega$ m |
| Thermal conductivity of electrode | 1.6 | 1/Wm K |
| Thermal conductivity of membrane | 0.3 | 1/Wm K |
| Catalyst loading | $4.0 \times 10^{-3}$ | kg $m^2$ |
| Catalyst surface area per unit mass | $1.0 \times 10^5$ | $m^2$ kg |
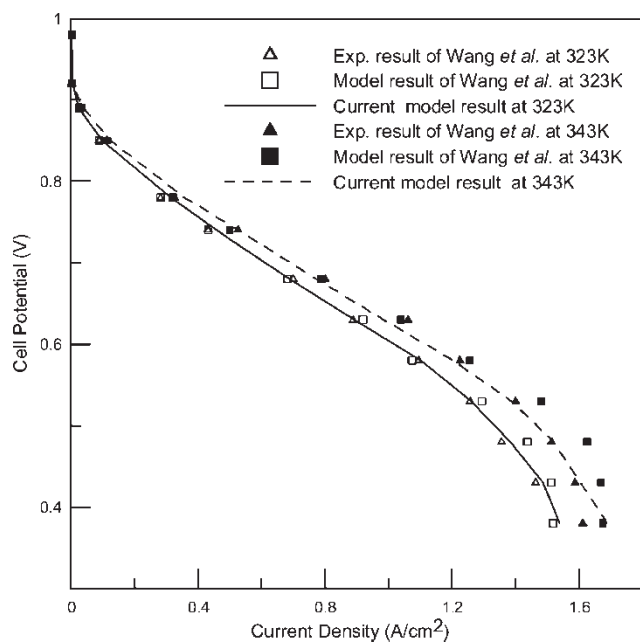


**Fig. 2** Comparison of current model results with Wang et al.'s report [30]. The humidification temperatures are 343 K and backpressures are 3 atm on anode and cathode sides

# 3 RESULTS AND DISCUSSION

A series of numerical simulations of underlying factors addressed in this study followed the modelling validation assessment. Prediction results presented are two-fold: those based on equal cell boundary temperatures on both sides while reactant humidification temperatures are altered and those based on equal temperatures of boundary and humidification on each side with a temperature gradient imposed between both sides. To examine the interrelation between the two main factors considered, humidification level and cell boundary temperatures varied from higher values (353–363 K) to lower values (333 to 323 K). This differs from previous studies with only one parameter changed [**30**, **31**], and hence, a more vivid situation that simulates cell operation is expected.

Note that from previous section comparisons, current modelling captures satisfactory polarization curve characteristics at low or high temperature range. However, this study focuses the prediction in higher temperature region with perturbed values within 20 K because researchers are more interested in cell performance in this region [**13–17**]. Also, owing to extreme thinness of the domain, introducing excessive temperature discrepancy on both sides seems unusual and impractical.

## 3.1 Effects of humidification scheme

In regard to promoting proton transport through the membrane, proper water vapour concentration in the cell region is crucial. Enhanced or reduced humidification scheme results on one or both sides of channel inlet ports are first reported. Subscripts B, H, A, and C in the legend of Fig. 3 and the following figures represent boundary, humidification, anode, and cathode, respectively. A temperature difference of 10 K between cell and humidification level, either larger or smaller, is posted on designated positions.

Results between the anode-enhanced humidification scheme and the base cases with these four temperatures being equal are compared in Fig. 3. Three cell boundary temperatures 333, 343, and 353 K are considered. The data in Fig. 3 reveal a concentration polarization effect for this humidification scheme in higher current density. In addition, this decay onset depends on cell temperature, and at higher cell temperature this phenomenon appears earlier. As inlet gas is fully saturated depending on to the humidification level, the anode mixture temperature decreases from heat transfer with the cell solid phase, and saturation level in the anode is elevated because of water condensation. This causes
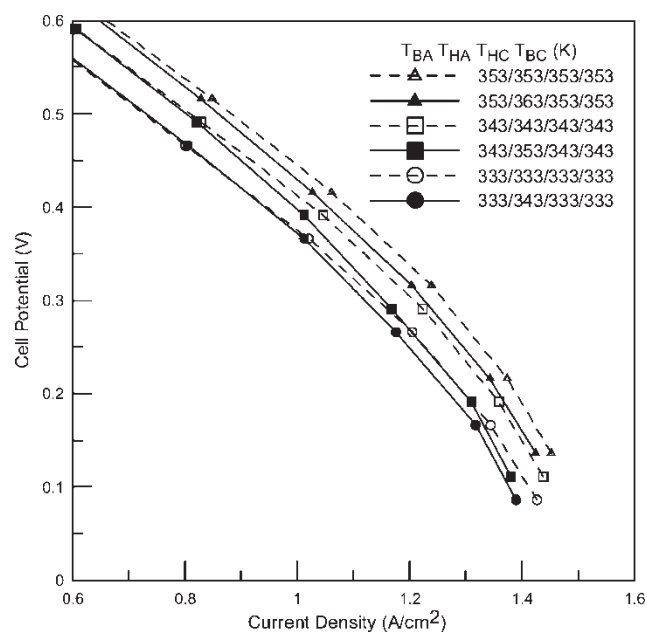


**Fig. 3** Effect of anode-enhanced humidification scheme with 10 K of anode humidification level greater than cell temperature for cell temperatures 333, 343, and 353 K

effective transport passage decrease of anode gas, promoting concentration overpotential. Another contributor to this is hydrogen depletion from the oxidation reaction in the anode CL, such that water partial pressure increases as well as condensation probability.

Cathode-enhanced humidification scheme influence with cathode mixture remained at 10 K greater than cell temperature as shown in Fig. 4. The results reveal a more serious concentration overpotential than the previous scheme; and the limiting current density decreases at higher cell temperature, i.e. cell performance dependence on temperature reversed at a high reaction rate for the present humidification scheme. Higher humidification temperature and corresponding low oxygen concentration in the inlet port may be considered to cause extra concentration overpotential at high cell temperature for this humidification scheme. However, reactant gas inlet velocity adjusts to alleviate dilution caused by high vapour concentration and satisfies the required stoichiometry as indicated in equation (20). In this context, high humidification level and water generation combined effect in the cathode reaction lead to a stronger effective porosity decay in the cathode electrode and decrease limiting current density at high cell temperature.

The simulation results for the anode-reduced humidification scheme are presented in Fig. 5. In this case, effect is found on the larger performance decay, compared with the base cases. This cell
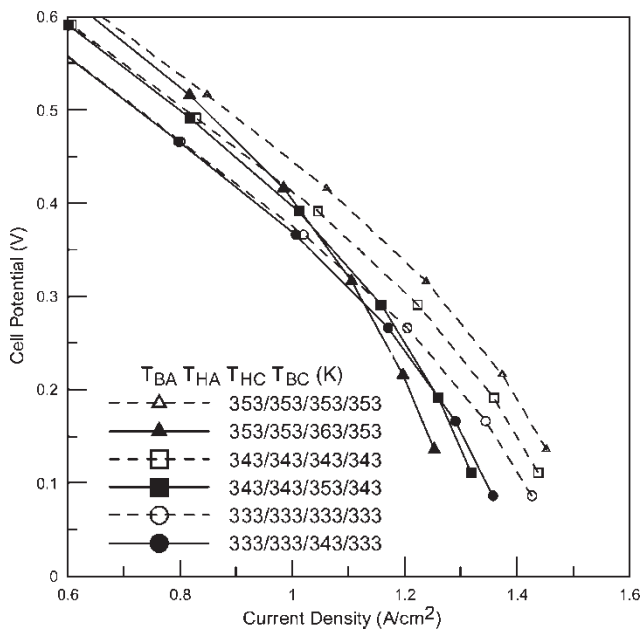
**Fig. 4** Effect of cathode-enhanced humidification scheme with 10 K of cathode humidification level greater than cell temperature for cell temperatures 333, 343, and 353 K

voltage reduction attributes to water swell deficiency in the membrane because of lower inlet water concentration. As the membrane conductivity is dictated by water content – the number of water molecules per fixed charged site – the supplied water vapour
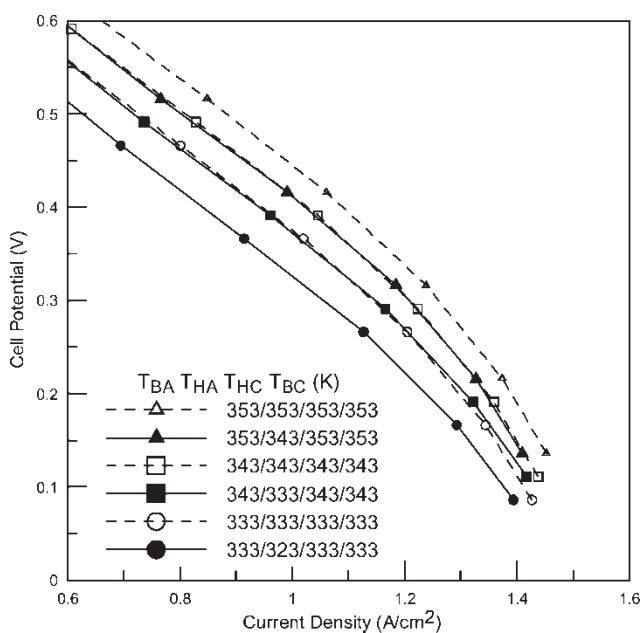
from anode inlet port is not enough to keep the membrane fully hydrated, such that the membrane proton transport is more difficult and activates a larger ohmic overpotential.

The cathode-reduced humidification scheme effect on cell output is shown in Fig. 6 for various cell temperatures. Comparing with base cases, it reveals the merit of applying the current scheme at a higher current density, causing cell voltage and performance increase at each cell temperature. Gas passage clogging prevention in the electrode is responsible for this gain because the produced water in the cathode reaction balances the lower inlet water concentration. However, an additional study (not shown in the figure) revealed that it reaches a plateau above cell temperatures of 348 K as large amounts of water generation exceed reduced humidity. For further improved performance, a larger humidification temperature reduction is needed to influence the membrane water content. In addition, at medium reaction rate and high cell temperature, cell resistance shows a slight variation. This is because the variation of membrane water content and conductivity arise from lower cathode water concentration.

To examine the impact of greater cell humidification gradient, the combined results of anode-reduced and cathode-enhanced humidification schemes are depicted in Fig. 7. The ohmic and concentration overpotentials clearly are all altered, compared with base cases. Cell performance in this
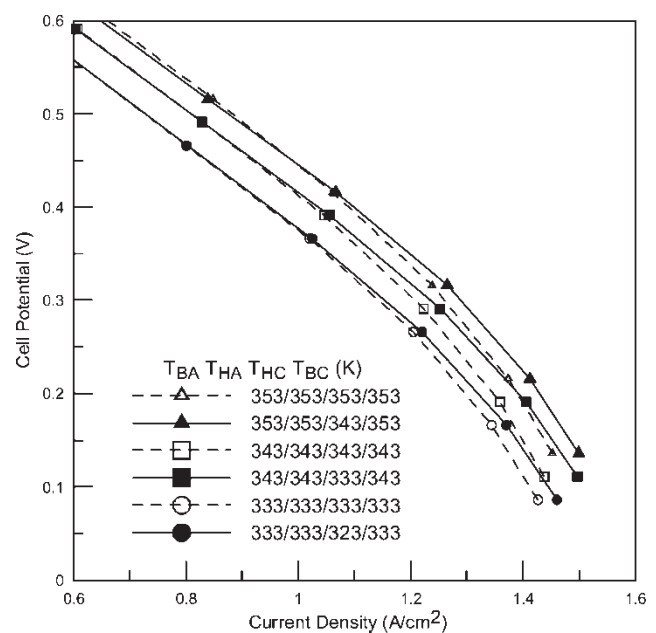


**Fig. 5** Effect of anode-reduced humidification scheme with 10 K of anode humidification level smaller than cell temperature for cell temperatures 333, 343, and 353 K



**Fig. 6** Effect of cathode-reduced humidification scheme with 10 K of cathode humidification level smaller than cell temperature for cell temperatures 333, 343, and 353 K
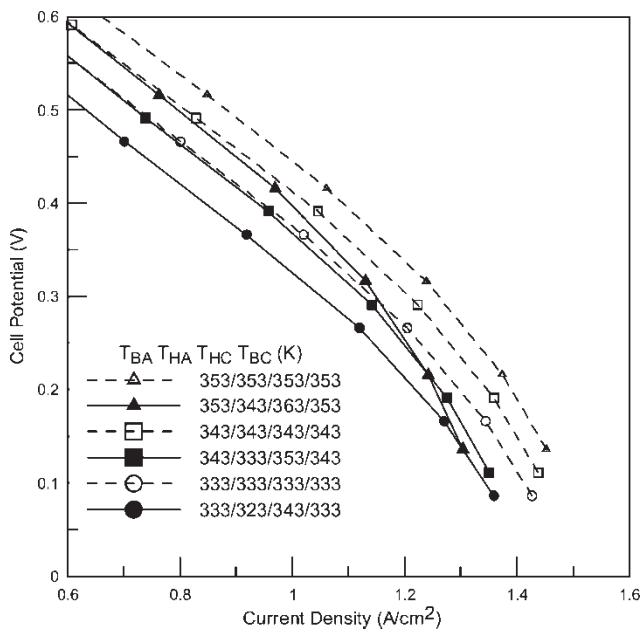
**Fig. 7** Effect of humidification gradient that combines anode-reduced and cathode-enhanced schemes for cell temperatures 333, 343, and 353 K



**Fig. 8** Performance curves with 353 K cathode temperatures and anode temperatures varied from 333 to 353 K

operating condition can be regarded as the individual scheme superposition. Nevertheless, the plot for 353 K exhibits a smaller decay at high reaction rate than the result in Fig. 4, as the reaction rate at the conduction-dominated region is suppressed from low anode humidity and the accompanying small membrane conductivity. Consequently, the series concentration overpotential at low cell voltage is slightly released. In a further study that reverses the humidification condition of the previous case, the same expected individual scheme superposition is shown. However, this effect is intrinsically non-linear because of complicated mechanisms of the coupled transport phenomena.

## 3.2 Effects of cell temperature gradient

Increasing cell bulk temperature reportedly creates a positive influence on cell performance [**30**]. Prediction results containing a series of boundary and humidification temperature variation on one electrode with others fixed are reported in this section. The reactants are also fully saturated based on boundary temperature. Polarization curves are plotted as total cell overpotential versus current density as cell temperature used in equation (22) cannot be obtained. Results with anode temperatures increased from 333 to 353 K at 353 K cathode temperatures are presented in Fig. 8. Cell current density does not change significantly until a higher reaction rate according to findings. Membrane conductivity
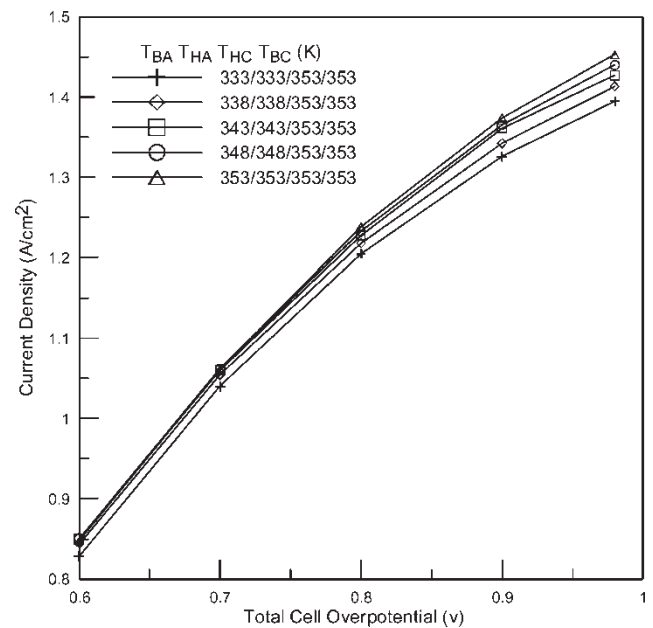
along central channel direction on the membrane middle plane is drawn in Fig. 9 at total cell overpotential of 0.98 V for further result information. It shows two influential factors for conductivity; the first is cell temperature with a positive effect. However, owing to the electro-osmotic drag transport process, water concentration decreases along the
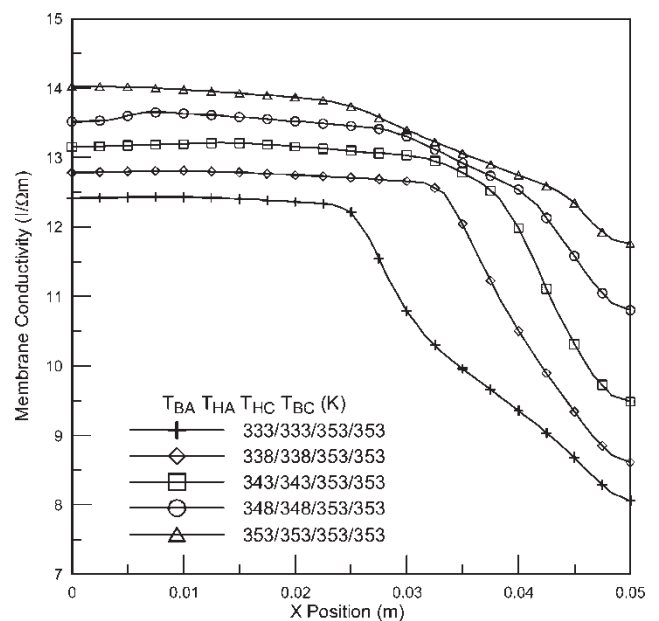


**Fig. 9** Membrane conductivity along central channel direction on the membrane middle section for cases in Fig. 8

anode channel, leading to a quicker membrane water content decay at 333 K anode temperature. Consequently, its current density exhibits a sensible decrease when compared with other higher anode temperature situations. A similar scenario with 333 K cathode temperature was also calculated. However, no appreciable cell performance variation is revealed. This can be explained by the anode kinetic independence with temperature, which leads to trivial cell output change.

The prediction result at 353 K anode temperature and continuous cathode temperature variation from 333 to 353 K is represented in Fig. 10. Obviously, the output current density increased monotonously with cathode temperature change, indicating that cell behaviour is dominated by the electrochemical reaction kinetics rather than conduction or concentration overpotentials. With sluggish cathode oxygen reduction, cathode exchange current density is several orders of magnitude smaller than the anode value, and a higher cathode temperature is beneficial for cell reaction and electricity generation.

Temperature gradient effect at low anode temperatures of 333 K and cathode temperature variation from 333 to 353 K are shown in Fig. 11. It indicates that current density dependence on cathode temperature variation has an entirely different tendency between medium and high cell reaction rates. Membrane conductivities along the central channel direction on middle section for total cell overpotentials of 0.5 V and 0.98 V are plotted in Fig. 12 for further information. When total cell overpotential is at
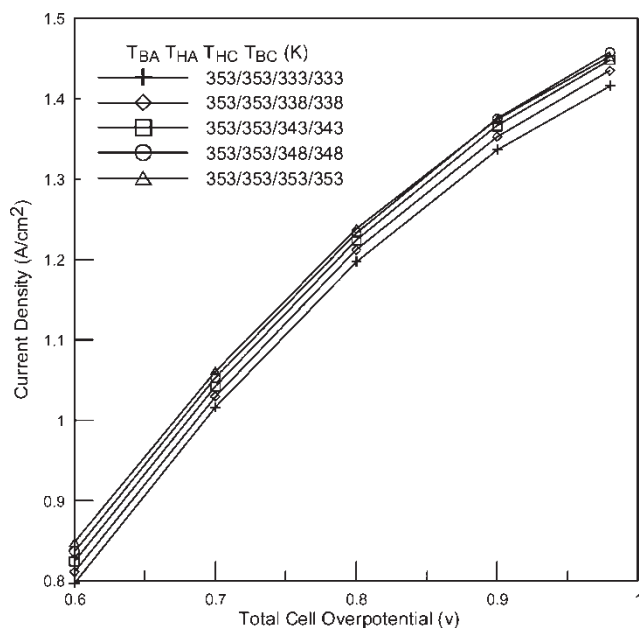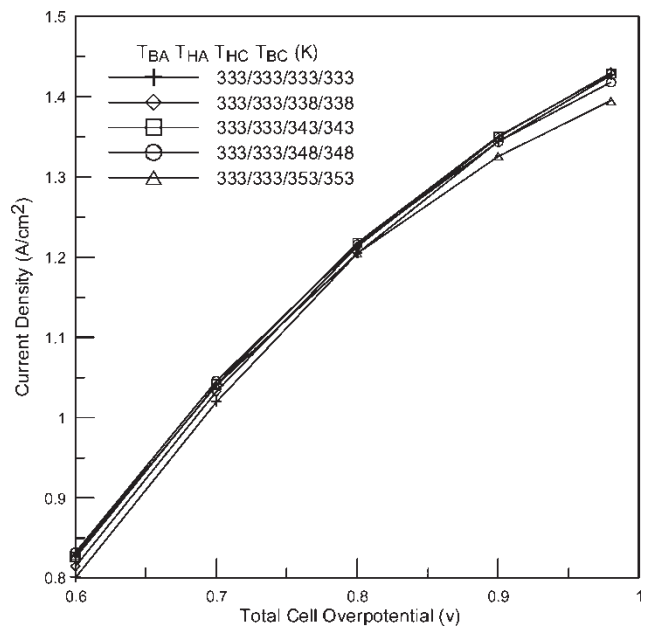


**Fig. 11** Performance curves with 333 K anode temperatures and cathode temperatures varied from 333 to 353 K

0.5 V, membrane conductivities are shown to be smaller than those of 0.98 V for various cathode temperatures. This can be explained by the smaller membrane water content for the former case with a weaker cell reaction and electro-osmotic drag. In addition, owing stronger cell reaction and water transport, membrane conductivity along the cell



**Fig. 10** Performance curves with 353 K anode temperatures and cathode temperatures varied from 333 to 353 K
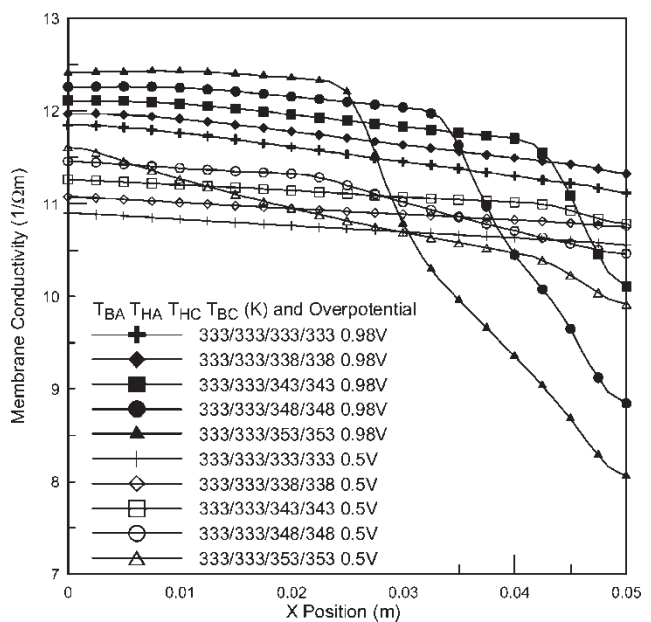


**Fig. 12** Membrane conductivity along central channel direction on the membrane middle section for cases in Fig. 11 at total cell overpotentials of 0.5 and 0.98 V
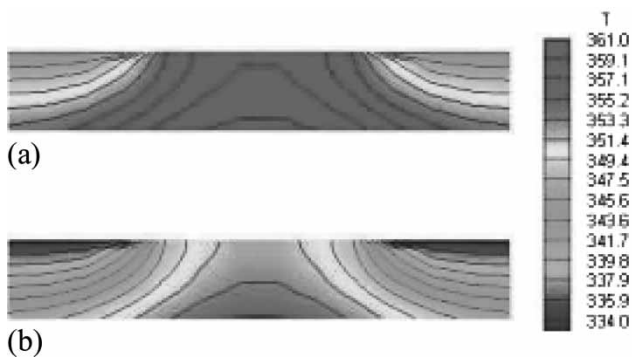
Fig. 13 Local temperature contours in cathode GDL at section of $x = 0.025$ m with 353 K anode temperatures and cathode temperatures (a) 343 K and (b) 333 K

channel has an earlier and more serious decay for overpotential at 0.98 V and 353 K cathode temperature. For this reason, it reverses the intrinsic relation between cell temperature and performance at high current density.

### 3.3 Local distributions of physical properties

Various temperature and humidification gradient effects on cell performance are previously presented. Displaying local physical property variations such as reactant concentration, temperature, and saturation level offers a more insightful understanding of the coupled transport phenomena in the PEMFC.

Temperature contours in cathode GDL at the $x = 0.025$ m section with 353 K anode temperatures and 343 and 333 K cathode temperatures are shown in Fig. 13. The total cell overpotential is at 0.8 V. The upper region of the plot is adjacent to the cathode channel and shoulders, whereas the lower boundary of the plot is connected to the CL. Obviously, as CL is the main source of heat generation, the highest temperature appears at the
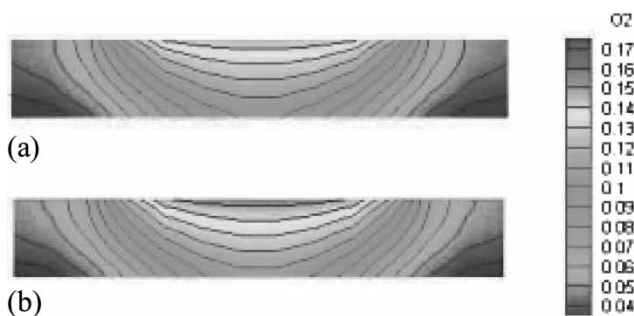


Fig. 14 Local oxygen mass fractions in cathode GDL at section of $x = 0.025$ m with 353 K anode temperatures and cathode temperatures (a) 343 K and (b) 333 K
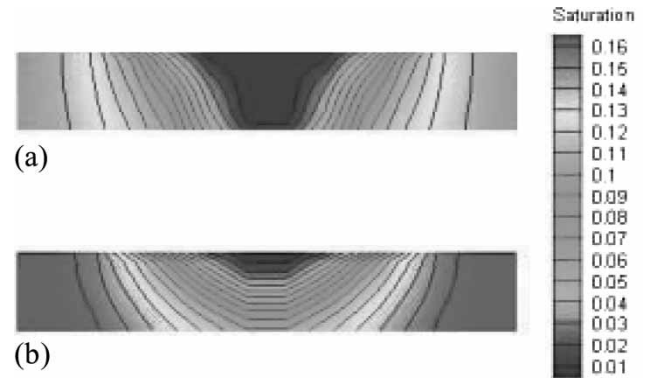


Fig. 15 Local water saturation in cathode GDL at section of $x = 0.025$ m with 353 K anode temperatures and cathode temperatures (a) 343 K and (b) 333 K

bottom of GDL. Meanwhile, on this CL interface, the central region exhibits greater temperature as the cathode BP and shoulder have more capability to dissipate heat than the channel.

The expected effect on cell physical properties is justifiable, given the temperature distribution. Local oxygen mass fractions for the previous cases are shown in Fig. 14. The data in this figure indicate that a higher GDL and CL temperature corresponds to lower oxygen concentration. This can be attributed to the higher reaction rate from equation (19) and greater membrane conductivity. More oxygen is consumed in the cell reaction as a result, and the local concentration is reduced.

Another temperature field influence can be observed in Fig. 15, which is the water saturation level in the GDL for the same scenarios. There are two important points that can be observed from this plot. First, as the transport direction is opposite to that of oxygen, the GDL shoulder region tends to accumulate more water vapour than the GDL channel region, leading to a higher saturation level at this location. Secondly, water vapour saturation pressure decreases at lower temperature, such that local water vapour partial pressure is apt to exceed saturation pressure. Consequently, the local saturation level increases with a 333 K cathode temperature. The further influence of this phenomenon is that reactant and product transport passages are hindered and the concentration overpotential is elevated.

### 4 CONCLUSIONS

A three-dimensional, non-isothermal numerical model has been developed to explore temperature gradient and humidification perturbation effects on

PEMFC. This model accounts for multi-component species transport and the two-phase flow. The CL local activation overpotential resolution is also achieved. According to the model prediction results and discussion, the following conclusions can be drawn.

1. The anode humidification level bears the impact of concentration and ohmic overpotentials on cell performance at elevated and reduced situations, respectively.
2. Proper cathode humidification level-reduction benefits cathode reactant transport and improves concentration polarization at a high reaction rate.
3. Despite its non-linear behaviour, a suitable PEMFC humidification scheme can be reached by carefully using the individual humidification level effect on either side of the cell.
4. Temperature gradient effect on cell performance exhibits entirely different behaviours depending on its direction and magnitude. When the cathode temperature is fixed at a lower level, the anode temperature variation has no noticeable change in the output current. However, when it is specified at a higher value, a larger temperature gradient is harmful at high current density.
5. Positive cell temperature gradient effect on its performance is found for medium reaction rate at a lower anode temperature. However, this trend is reversed at a higher reaction rate because of membrane dehydration.
6. Local physical property contours demonstrate interrelations among the temperature field, local oxygen concentration, and water saturation level. As a result, cell performance has a close connection with these property variations, and the essential role of existing PEMFC temperature and humidification gradients is elucidated.

## REFERENCES

**1 Spiegel, R. J., Gilchrist, T.,** and **House, D. E.** Fuel cell bus operation at high altitude. *Proc. Instn Mech. Engrs, Part A: J. Power and Energy*, 1999, **213**, 57–68.
**2 Nguyen, T.** and **White, R. E.** A water and heat management model for proton-exchange-membrane fuel cells. *J. Electrochem. Soc.*, 1993, **140**(8), 2178–2186.
**3 Zawodzinski, T. A., Derouin, C., Radzinski, S., Sherman, R. J., Smith, V. T., Springer, T. E.,** and **Gottesfeld, S.** Water uptake by and transport through Nafion 117 membrane. *J. Electrochem. Soc.*, 1993, **140**(3), 1041–1047.
**4 Siegel, N. P., Ellis, M. W., Nelson, D. J.,** and **von Spakovsky, M. R.** A two-dimensional computational model of a PEMFC with liquid water transport. *J. Power Sources*, 2004, **128**, 173–184.
**5 Voss, H. H., Wilkinson, D. P., Pickup, P. G., Johnson, M. C.,** and **Basura, V.** Anode water removal: a water

management and diagnostic technique for solid polymer fuel cells. *Electrochim. Acta*, 1995, **40**(3), 321–328.
**6 Wood, D. L., III, Yi, J. S.,** and **Nguyen, T. V.** Effect of direct liquid water injection and interdigitated flow field on the performance of proton exchange membrane fuel cells. *Electrochim. Acta*, 1998, **43**(24), 3795–3809.
**7 Bernardi, D. M.** Water-balance calculation for solid-polymer-electrolyte fuel cells. *J. Electrochem. Soc.*, 1990, **137**(11), 3344–3350.
**8 Bernardi, D. M.** and **Verbrugge, M. V.** Mathematical model of a gas diffusion electrode bounded to a polymer electrolyte. *AIChE J.*, 1991, **37**(8), 1151–1163.
**9 Bernardi, D. M.** and **Verbrugge, M. W.** A mathematical model of the solid-polymer-electrolyte fuel cell. *J. Electrochem. Soc.*, 1992, **139**(9), 2477–2491.
**10 Springer, T. E., Zawodzinski, T. A.,** and **Gottesfeld, S.** Polymer electrolyte fuel cell model. *J. Electrochem. Soc.*, 1991, **138**(8), 2334–2342.
**11 Fuller, T. F.** and **Neuman, J.** Water and thermal management in solid-polymer-electrolyte fuel cells. *J. Electrochem. Soc.*, 1993, **140**(5), 1218–1225.
**12 Yi, J. S.** and **Nguyen, T. V.** An along-the-channel model for proton exchange membrane fuel cells. *J. Electrochem. Soc.*, 1998, **145**(4), 1149–1159.
**13 Rowe, A.** and **Li, X.** Mathematical modeling of proton exchange membrane fuel cells. *J. Power Sources*, 2001, **102**, 82–96.
**14 Baschuk, J. J.** and **Li, X.** Modeling of polymer electrolyte membrane fuel cells with variable degree of water flooding. *J. Power Sources*, 2000, **86**, 181–196.
**15 Simpalee, S.** and **Dutta, S.** Numerical prediction of temperature distribution in PEM fuel cells. *Numer. Heat Trans. Part A*, 2000, **38**, 111–128.
**16 Djilali, N.** and **Lu, D.** Influence of heat transfer on gas and water transport in fuel cells. *Int. J. Therm. Sci.*, 2002, **41**, 29–40.
**17 Ju, H., Meng, H.,** and **Wang, C. Y.** A single-phase, non-isothremal model for PEM fuel cells. *Int. J. Heat Mass Trans.*, 2005, **48**, 1303–1315.
**18 Wangard, W., III, Dandy, D. S.,** and **Miller, B. J.** A numerical stable method for integration of the multi-component species diffusion equations. *J. Comp. Phys.*, 2001, **174**, 460–472.
**19 Cussler, E. L.** *Diffusion mass transfer in fluid system*, 2nd edition, 1997 (Cambridge University Press, Cambridge).
**20 Gurau, V., Barbier, F.,** and **Liu, H. T.** An analytical solution of a half-cell model for PEM fuel cell. *J. Electrochem Soc.*, 2000, **147**(7), 2468–2477.
**21 Wang, C. Y.** and **Cheng, P.** Multiphase flow and heat transfer in porous media. In *Advance in heat transfer* (Eds J. P. Hartnett, T. F. Irvine, Jr, Y. I. Cho, and G. A. Greene), 1997 (Acadmic Press, San Diego).
**22 Mazumder, S.** and **Cole, J. S.** Rigorous 3-D mathematical modeling of PEM fuel cells II. Model predictions with liquid water transport. *J. Electrochem. Soc.*, 2003, **150**(11), A1510–A1517.
**23 Wang, C. Y.** and **Beckermann, C.** A two-phase mixture model of liquid–gas flow and heat transfer in capillary porous media-I. Formulation. *Int. J. Heat Mass Trans.* 1993, **36**(11), 2747–2758.

24 **He, W., Yi, J. S.,** and **Nguyen, T. V.** Two-phase flow model of the cathode of PEM fuel cells using interdigitated flow fields. *AIChE J.*, 2000, **46**(10), 2053–2064.

25 **Parthasarathy, A., Srinivasan, S.,** and **Appleby, A. J.** Temperature dependence of the electrode kinetics of oxygen reduction at the platinum/nafion interface-a microelectrode investigation. *J. Electrochem. Soc.*, 1992, **139**(9), 2530–2537.

26 **Nguyen, P. T., Berning, T.,** and **Djilali, N.** Computational model of a PEM fuel cell with serpentine gas flow channels. *J. Power Sources*, 2004, **130**, 149–157.

27 **Hwang, J. J., Chen, C. K., Savinell, R. F., Liu, C. C.,** and **Wainright, J.** A three-dimensional numerical simulation of the transport phenomena in the cathodic side of a PEMFC. *J. Appl. Electrochem.*, 2004, **34**, 217–224.

28 **Hu, G., Fan, J., Chen, S., Liu, Y.,** and **Cen, K.** Three-dimensional numerical analysis of proton exchange membrane fuel cells (PEMFCs) with conventional and interdigitated flow fields. *J. Power Sources*, 2004, **136**, 1–9.

29 **Patanker, S. V.** *Numerical heat transfer and fluid flow*, 1st edition, 1980 (Hemisphere, New York).

30 **Wang, L., Husar, A., Zhou, T.,** and **Liu, H.** A parametric study of PEM fuel cell performances. *Int. J. Hydrogen Energy*, 2003, **28**, 1263–1272.

31 **Berning, T.** and **Djilali, N.** Three-dimensional computational analysis of transport phenomena in a PEM fuel cell – a parametric study. *J. Power Sources*, 2003, **124**, 440–452.

## APPENDIX

### Notation

| | |
|---|---|
| $A$ | surface area of the catalyst particle ($m^2$) |
| $c$ | molar concentration ($mol/m^3$) |
| $C$ | form drag constant |
| $\boldsymbol{D}$ | multi-component diffusion coefficient ($m^2/s$) |
| $D$ | binary diffusion coefficient ($m^2/s$) |
| $F$ | Faraday constant (96 500 C/mol) |
| $g$ | gravitational acceleration ($m/s^2$) |
| $h$ | enthalpy (J/kg) |
| $H$ | height (m) |
| $\boldsymbol{i}$ | vector of current density ($A/m^2$) |
| $i$ | current density ($A/m^2$) |
| $I$ | reference current density ($A/m^2$) |
| $k$ | relative permeability |
| $K$ | permeability ($m^2$) |
| $L$ | length (m) |
| $m$ | catalyst loading ($kg/m^3$) |
| $M$ | molecular weight (kg/mol) |
| $n$ | number of species |
| $N$ | flux ($kg/m^2/s$) |
| $P$ | pressure (Pa) |
| $q$ | number of electron transferred |
| $r$ | rate constant ($s^{-1}$ or 1/atm s) |
| $R$ | universal constant (8.314 J/mol/K) |

| | |
|---|---|
| $s$ | saturation level |
| $S$ | source term |
| $T$ | temperature (K) |
| $\boldsymbol{U}$ | fluid velocity (m/s) |
| $v$ | inlet velocity (m/s) |
| $w$ | mass fraction |
| $W$ | width (m) |
| $x$ | molar fraction |
| | |
| $\beta$ | transfer coefficient |
| $\gamma$ | water content in membrane |
| $\delta$ | tortuosity |
| $\varepsilon$ | porosity |
| $\varsigma$ | surface tension (N/m) |
| $\eta$ | overpotential (V) |
| $\theta$ | contact angle ($°$) |
| $\kappa$ | thermal conductivity (W/m/K) |
| $\lambda$ | relative mobility |
| $\mu$ | dynamic viscosity (N s/m) |
| $\nu$ | kinematic viscosity ($m^2/s$) |
| $\xi$ | stoichiometry of hydrogen or oxygen |
| $\rho$ | density ($kg/m^3$) |
| $\sigma$ | electrical conductivity ($1/\Omega$ m) |
| $\boldsymbol{\tau}$ | shear stress tensor ($N/m^2$) |
| $\phi$ | potential (V) |
| $\varphi$ | concentration dependence |
| $\psi$ | collision diameter (Å) |
| $\Omega$ | collision integral |

*Superscripts*

| | |
|---|---|
| c | capillary |
| eff | effective value |

*Subscripts*

| | |
|---|---|
| a | anodic |
| BA | boundary of anode side |
| BC | boundary of cathode side |
| c | cathodic |
| cat | catalyst |
| cel | cell |
| cha | channel |
| con | condensation |
| eva | evaporation |
| F | Forchheimer term |
| g | gas |
| h | enthalpy |
| HA | humidification of anode side |
| HC | humidification of cathode side |
| in | inlet |
| j | volumetric transfer current density |
| k | anode or cathode |
| l | liquid |

| m   | momentum                         | ref | reference                |
|-----|----------------------------------|-----|--------------------------|
| mas | per unit mass of catalyst carbon | s   | species                  |
| mem | membrane phase of the cell       | sat | saturation               |
| n   | hydrogen or oxygen               | sol | solid phase of the cell  |
| oc  | open circuit value               | tot | total                    |
| plt | platinum                         | v   | per unit volume          |
| r   | relative                         | w   | water                    |